Bio-inspired carbon doped graphitic carbon nitride with booming photocatalytic hydrogen evolution

Luhong Zhang[a], Zhengyuan Jin[a], Shaolong Huang[a], Xiaoyong Huang[b,*], Binghui Xu[c], Liang Hu[a], Hongzhi Cui[d], Shuangchen Ruan[a], Yu-Jia Zeng[a,*]

[a] *Shenzhen Key Laboratory of Laser Engineering, Key Laboratory of Optoelectronic Devices and System of Ministry of Education and Guangdong Province, College of Optoelectronic Engineering, Shenzhen University, Shenzhen, 518060, China*
[b] *College of Physics and Optoelectronics, Taiyuan University of Technology, Taiyuan, 030024, China*
[c] *School of Materials Science and Engineering, Qingdao University, Qingdao, 266071, China*
[d] *College of Civil Engineering, Shenzhen University, Shenzhen, 518060, China*

ARTICLE INFO

ABSTRACT

In this work, kapok fiber (KF), known as a versatile biomass, has been mixed with melamine to produce carbon modified graphitic carbon nitride (CCN) by one-step pyrolysis. The bio-char ribbon edges formed after the decomposition of KF act as the substrate for the epitaxial growth of CCN. The photocatalytic activity in hydrogen (H_2) generation from water splitting has been investigated. Nash Equilibrium from Game Theory has been firstly applied in the analysis of the H_2 generation rates among catalysts. The bio-char ribbon edges at the thin CN layers after carbon doping from KF decomposition improve the charge separation and transfer for the surface H_2 generation reaction. The CCN exhibits superior visible-light-driven photocatalytic activity and the H_2 evolution rate (18.89 μmol/h) is 67.5 times higher than that of the pristine CN (0.28 μmol/h). The apparent quantum yields are calculated to be 4.1%, 1.4%, 0.66% for monochromatic light λ = 420, λ = 470 and λ = 550 nm, respectively.

1. Introduction

Photocatalysis based on semiconductors (TiO_2 [1–3], ZnO [4–8], CdS [9–11], $BiVO_4$ [12,13] and so forth) have great potential to solve the energy dilemma and environmental issues. Graphitic carbon nitride (CCN), a fascinating conjugated polymer semiconductor, has received tremendous attention in the recent decade [14,15]. As an earth-abundant, inexpensive, robust, metal-free and visible-light-responsive photocatalyst, CN is a promising candidate to convert the solar light into the chemical energy via catalytic reaction such as water-splitting H_2 evolution [16] and CO_2 reduction [17]. However, the pristine CN is usually limited by unsatisfactory photocatalytic efficiency, which is ascribed to the high recombination rate of charge carriers, the low electrical conductivity and the lack of absorption above 460 nm [18,19]. Establishment of heterojunction [20–25], modification such as doping and copolymerization are effective strategies to optimize the photoactivity by tuning the crystallographic, electronic structure and energy band configuration [26]. In particular, nonmetal doping such as carbon doping appears promising. Highly promotive photocatalytic activity has been realized upon carbon quantum dots doped CN, where

carbon dots are prefabricated before doping [14,26–30]. Chemical carbon sources such as macromolecule polyacrylamide [31], glucose [32], saccharide [33], and cellulose acetate [34] have also been utilized to prepare carbon doped CN. However, there are limited reports on the biomass as the carbon source for the synthesis of carbon doped CN.

Nature is the biggest material manufacturer, where we can find the prototype of artificial materials' morphologies, such as core-shell, flower-like, honeycomb, tube or fiber structures etc. So, in the aspect of material design, researchers tend to mimic the nature or search bio-template from nature. Kapok fiber (KF) is a versatile biomass material, mostly utilized as stuffing for upholstery, bedding, acoustic and thermal insulation, also as a filling for jackets and life belts. Recently, KF is getting more and more extensive attention in research and application because of its excellent natural characteristics such as its lightness, super warmth, anti-bacterial, anti-mite etc. Unlike cotton and artificial fiber, KF has the highest hollow ratio of 97% (with an inner diameter of ˜14 μm), which can provide a larger accessible surface and faster transfer channel [35]. Mohamad and co-workers [36] used KF as both bio-template and carbon resource to synthesis carbon doped CN which exhibited improved photocatalytic degradation property. In their work,

---

urea served as the precursor for the synthesis of CN. However, as we know although CN derived from urea possesses a high surface area, the yield rate is very low (approximately 4%) [16]. Bulk CN obtained from melamine can get a much higher yield rate (approximately 60%). Therefore, CN derived from melamine is more suitable for the industrial application. However, the relatively low surface area of pristine CN derived from melamine causes the poor photocatalytic activity and hinders its industrial prospects [34].

Herein, KF has been utilized in pyrolysis with melamine, where KF plays double roles acting as the carbon source and the substrate for the epitaxial growth of CN. Moreover, the nano-biochar ribbon edges derived from KF provide the channel for the fast electron transfer and improve the photocatalytic activity. Specifically, compared with pristine CN, the optimal sample exhibits more than sixty-sevenfold improvement of the photocatalytic H_2 evolution under visible light. Considerable apparent quantum yields are realized to be 4.1%, 1.4%, 0.66% for monochromatic light $\lambda = 420$, $\lambda = 470$ and $\lambda = 550$ nm, respectively. Therefore, the absorption and utilization of sunlight above 460 nm for CN are significantly improved in this work. To the best of our knowledge, this novel carbon modified CN composites obtained from one step pyrolysis of KF and melamine are utilized for the first time in the H_2 evolution reaction. Hence, this high H_2 evolution rate in our work open a new perspective to utilize the KF as a cost-effective, biocompatible, eco-friendly carbon source in catalysis.

2. Experimental

2.1. Sample preparation

All chemicals were reagent grade and used without further purification. Melamine (99%) andsodium chlorite (80%) were purchased from Aladdin, China. Kapok fibers were collected from the Houhai Campus of Shenzhen University.

2.2. Fabrication of bulk graphitic carbon nitride and carbon modified graphitic carbon nitride

For bulk CN, melamine (2 g) was put into an alumina crucible with a lid, calcined in a muffle furnace with air atmosphere under 550 °C, 600 °C 650 °C for 3 h (heating rate of 2 °C/min). After cooling down to the room temperature, the obtained samples were finely ground into powders, which were named CN550, CN600, and CN650 accordingly.

For CCN, KF was washed with ethanol and dried at 60 °C overnight before use. Then, melamine (2 g) and KF (weight percentage of 0.5–7.5 to melamine) were immersed in 10 ml ethanol and mixed in alumina crucibles. Note that with further increase of the KF, it became difficult to ground the composite into powder due to the high content of carbonated fiber. After drying in an oven at 60 °C overnight, crucibles with lids were transferred to the muffle furnace under calcination with an air atmosphere at 550 °C, 600 °C, and 650 °C for 3 h. (With the heating rate of 2 °C/min). After naturally cooling down to the room temperature, the obtained samples were finely ground into powders. The samples were labeled as xCCNy (x = weight percentage of added KF, y = calcination temperature.)

Note that the KF was also pre-treated to remove the surface paraffin according to reports [35,36]. A certain amount of KF was immersed in 3 wt% $NaClO_2$ solution for one day then under magnetic stirring for 10 min and then finally centrifuged by washing with ultrapure water 3 times and ethanol before dried overnight in an oven at 60 °C. The $NaClO_2$ pre-treated KF was named as t-KF.

To study the influence of surface biomass wax on the carbonization of KF and the pyrolysis of melamine, t-KF was also used in the preparation of CCN. And then the CCN prepared from t-KF was named xtCCNy in this work. (x = weight percentage of added t-KF, y = calcination temperature.) Additionally, CN modified with the paraffin (which is the main component of the surface biomass wax) was also

prepared. In detail, a certain volume of paraffin was added and mixed with melamine then transferred into alumina crucible with the cover on, followed by calcination at 600 °C for 3 h (with a heating rate of 2 °C/min). Finally, the product was collected and named CCN(M + P)600.

3. Photocatalytic activity measurement

3.1. H_2 generation from water splitting

There are two major photocatalytic approaches for H_2 evolution from water splitting, i.e. direct photocatalytic water splitting and photoelectrochemical water splitting. Compared with the direct H_2 generation by photocatalysis, photoelectrochemical water splitting is still facing the challenge in the fabrication of high-quality CN thin films [37–39]. The H_2 evolution rate therefore varies to a large extent by different preparation methods [38]. On the other hand, the experimental conditions are relatively controllable for direct photocatalytic water splitting. Therefore, the H_2 generation in this work was conducted via direct photocatalytic water splitting.

In detail, 10 mg of the obtained samples, 10 mL triethanolamine (TEOA) and 100 μL H_2PtCl_6 solutions (Pt, 3 g/L) were mixed and diluted with ultrapure water to 100 mL. After sonication for 10 min, the solution was transferred to the reaction cell and vacuumed with constant stirring. The temperature of the reaction solution was carefully maintained with circulating cooling water at 6 °C during the whole experiment. Xe lamp (CEAULIGHT, CEL-HXF30) was the light source, a 420 nm cut filter (CEAULIGHT, CEL-UVIRCUT420) was used (light intensity in the bottom center was adjusted to 100 mW/cm^2). The generated H_2 was monitored by gas chromatography (TCD, CEAULIGHT, GC-7920) every 30 min with ultrapure N_2 worked as the carrier gas.

For the measurement of the apparent quantum yield (AQY), the aforementioned H_2 liberation from water splitting was proceeded under Xe lamp (CEAULIGHT, CEL-HXF300) with 420, 470 and 550 band-pass filter respectively (CEAULIGHT, CEL-QD420, CEL-QD470 and CEL-QD550), which emitted light at wavelength of ca. 420, 470 and 550 nm respectively. The catalyst was irradiated for 6 h, the average light intensity of irradiation was determined to be 10 mW/cm^2 and the irradiation area was 10.17 cm^2. The AQY was calculated by using the equation:

$$\eta_{AQY} = \frac{N_e}{N_p} = \frac{2 \times M \times N_A}{\frac{E_{total}}{E_{photo}}} \times 100 \% = \frac{2M \times N_A}{\frac{S \times P \times T}{h \times \frac{c}{\lambda}}} \times 100 \%$$

$$= \frac{2 \times M \times N_A \times h \times c}{S \times P \times T \times \lambda} \times 100\%$$

Where, Ne is the number of converted electrons, Np is the number of incident photons. M is the amount of H_2 molecules (mol), N_A is Avogadro constant (6.02×10^{23} /mol), h is the Planck constant (6.63×10^{-34} m^{2}kg/s), c is the speed of light (3×10^8 m/s), S is the irradiation area (cm^2), P is the intensity of irradiation light (W/cm^2), T is the photoreaction time (s), λ is the wavelength of the monochromatic light (m).

3.2. Photoelectrochemical measurement

The obtained samples were loaded on FTO substrates by the electrophoresis method. 10 mg of the sample and a grain of iodine were ultrasonically dispersed in 20 ml acetone solution. Two FTO conducting glasses were placed in the solution as the anode and the cathode. A bias of 30 V was applied between the two electrodes for 3 min (3 times). The FTO with 1.5×1.5 cm^2 area of the loaded sample was then dried on the electric furnace at 350 °C for 4 h before it was used for photoexcitation experiment.

The photocurrent was measured on a CHI 660E electrochemical workstation with a three-electrode system, in which the prepared electrode, a Pt (CH Instruments, Inc.) and an Ag/AgCl (CH Instruments,

Inc.) electrode was used as the working electrode, the counter electrode and the reference electrode, respectively. 0.5 M Na_2SO_4 solution was used as the electrolyte. A Xe lamp (CEAULIGHT, CEL-HXF300) with Air Mass 1.5 G illumination filter (CEAULIGHT, CEL-AM 1.5) was used as the light source. The light intensity of the light source was kept to 21.5 mW by adjusting the distance between the light source and the sample.

3.3. Characterization

X-ray diffraction (XRD) patterns were measured on a Rigaku Ultima IV X-ray diffractometer under Cu-Kα radiation (λ = 0.15418 nm). Functional group vibrations were confirmed by using a Fourier transforms infrared spectrometer (FTIR; Thermol scientific Nicolet iz10, in 10). Surface chemical states were investigated by X-ray photoelectron spectroscopy (XPS) measurement with Thermol Scientific ESCALAB 250Xi system and adventitious C1s peak (284.6 eV) as the reference. The morphology and microstructure of the samples were characterized by a field-emission scanning electron microscope (FESEM, JEOL JSM-7800 F) equipped with an energy dispersive X-ray spectrometer (EDS), a transmission electron microscope (TEM, JEOL JEM-2100 Plus), and the Bruker MULTIMODE atomic force microscope (AFM). The thermogravimetric-differential scanning calorimetry (TG-DSC) for the precursors and the thermogravimetric analysis (TGA) of the photocatalysts were measured by a Mettler Toledo TGA/DSC thermal gravimetric analyzer in the argon and air respectively, with a heating rate of 10 °C/min. N_2 adsorption-desorption isotherms were recorded with an Autosorb-IQ-MP/XR surface area and pore analyzer (Quantachrome). Specific surface areas were calculated with the Brunauer-Emmett-Teller (BET) model using nitrogen adsorption data obtained in between P/P_0 = 0.05-0.35. The Barrett-Joyner-Halenda (BJH) model was utilized for determining the pore size distributions based on the desorption branch of the N_2 isotherms. Diffuse reflectance spectra (DRS) were measured using a UV–vis spectrophotometer (PerkinElmer, LAMBDA) equipped with an integrating sphere unit. Fluorescence spectra were obtained using a photoluminescence spectrometer (Shimadzu, RF-5301PC; 325 nm as the incident light source). Electron spin resonance (ESR) of radicals spin-trapped by 5, 5-dimethyl-1-pyrroline N-oxide (DMPO) was recorded on an ER200-SRC-10/12 spectrometer. Samples for ESR measurement were prepared by mixing the samples in 10 ppm DMPO (aqueous/ methanol) solution and were irradiated with visible light for 10 min.

4. Result and discussion

A schematic for the preparation of CCN is shown in Fig. 1. Melamine and KF are mechanically mixed first. Then during the programmed heating process, the KF is undergoing shrinking and carbonizing into the nano-biochar ribbons. The shrinkage and carbonization occur at 130 °C and 230 °C, respectively, as indicated in the thermal absorption in Fig. 2b. Simultaneously, the monomer melamine polymerizes into the melem at around 230 °C, as indicated in Fig. 2a. During the heating process, the linkages are generated between melem and nano-biochar ribbon. With continuous heating, the melem self-assembles into CN on

the nano-biochar ribbon substrate. As we can see, the complete carbonization of KF and the formation of CN happen at the same temperature at approximately 350 °C. So, we suppose that the CCNs are obtained by the epitaxial growing on the nano-biochar ribbons at the final heating stage. This hypothesis can be confirmed by the TG-DSC of the precursors in Fig. 2 The KF becomes ash at 500 °C. With further heating, the generated CN starts to decompose at 550 °C and then completely decomposes at 740 °C in the argon. When the CCN composites are used into photocatalytic hydrogen evolution, upon visible-light irradiation, the holes (h^+) generated on the carbon modified CN are consumed by sacrificial agent TEOA. Meanwhile, the generated electrons are transferred to the nano-biochar ribbon edge and then migrate to the Pt for the immediate H_2 evolution.

4.1. Physical and chemical properties characterization

To detect the crystal structure and phase information of the CCN samples, XRD measurements were carried out. As shown in Fig. 3a, the (100) and (002) diffraction peaks of CN550, CN650 and 0.5CCN650 at about 13.1° and 27.5° can be associated with the repeated tri-s-heterocycle packing in the conjugated CN planes and the interlayer stacking of graphite-like materials, respectively [40]. Compared with CN550, the peaks of CN650 and 0.5CCN650 become weaker. This is mainly attributed to the disorder in the in-plane repeated packing of CN, which is a typical feature of amorphous CN [41,42]. Additionally when the calcination temperature increases from 550 to 650 °C, the (002) peak shifts to the higher degree. More functional group branches are generated after the pyrolysis at higher temperatures, which is also supported by FTIR (Fig. 4). Therefore, hydrogen bonds and conjugated double bonds from branches can enhance the interaction between layers. As a result, the interlayer distance decreases for CN650 and 0.5CN650. Note that the loading of KF does not change the interlayer distance for CN. As we can see in Fig. 3b, the characteristic (002) peak does not shift but decreases in intensity along with the increase in the amount of KF. Therefore, the increase in the amount of KF aggravates the amorphous degree of CN, which may boom the photocatalytic activity.

Fig. 4 shows the FTIR spectra for the CNs and CCNs samples. Typically, the broad vibration bands at 3000–3500 cm^{-1} belong to O−H and N−H stretching vibrations, suggesting the partial hydrogenation of nitrogen atoms on the edges of CN layers [43]. Several vibration bands at 1000–1700 cm^{-1} are attributed to the CN stretching vibrations in the CN heterocycles [44]. More vibration brands are generated after the CN prepared at higher temperatures, indicating the partial amorphism of CN and more functional group branches are generated after the pyrolysis at a higher temperature. The band at 814 cm^{-1} originates from the vibration mode of the s-triazine unit. Clearly, CCN and CN give the similar FTIR signals, indicating that the introduction of KF during the pyrolysis of melamine does not alter the formation of the chemical structure for CN.

Fig. 5a shows the survey XPS spectra for 0.5CCN650 and CN550 samples. Only C, N and O atoms are detected in both samples. The C and O atom ratios for 0.5CCN650 are higher than those from CN550, revealing that the C doping is realized after the KF modification.
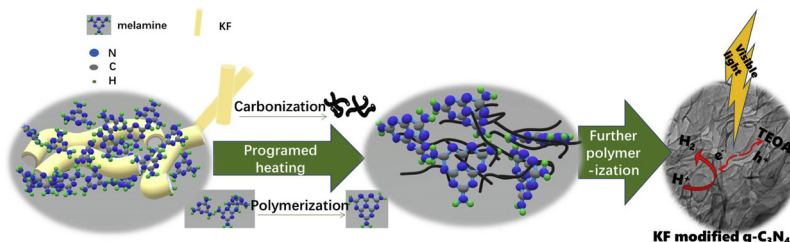

Fig. 1. Schematic for the fabrication of KF modified graphitic carbon nitride (CCN), which is prepared via a facile one-step pyrolysis approach.
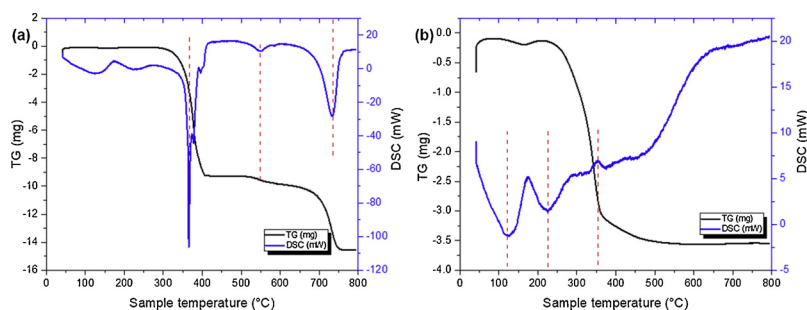
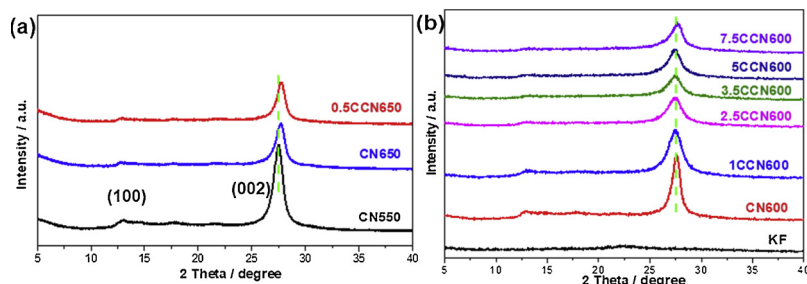**Fig. 2.** The TG-DSC for precursors (a) Melamine (b) KF.

Fig. 3. (a) XRD patterns for the CN550, CN650 and 0.5CCN650; (b) the crystal patterns change along the increase in KF amount for CCN samples prepared at 600 °C.
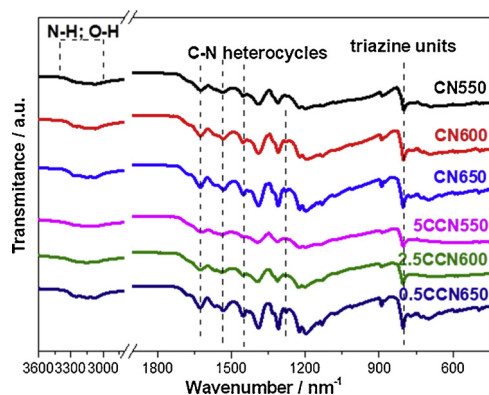

Fig. 4. FTIR spectra for CN550, CN600, CN650 samples, and the KF modified samples: 5CCN550, 2.5CCN600 and 0.5CCN650.

Furthermore, the higher O content implies the partial amorphism and functionalization. The higher O concentration in 0.5 CCN650 (6.92%) compared with CN550 (1.52%) reflects that more absorbed O_2, −OH and C=O generated on the edge of CN cycle (Fig. 5b), which is consistent with the chemical structure signals from the XRD and FTIR. Fig. 5c and 5d are the high-resolution spectra for C and N, respectively. In Fig. 5c, 0.5CCN650 exhibits three C1s binding energies of around 284.6, 286.3 and 288.1 eV which are corresponding to bonding states of carbon species, i.e. C−C, C−OH and N−C=N, respectively. In contrast, only C−C (284.6 eV) and N−C=N (288.0 eV) deconvolution peaks are obtained for the C1s in CN550, which is in good agreement with the sole absorbed O_2 peak for CN550 in Fig. 5b. In Fig. 5d, the main peaks of N1s binding energies are located approximately at 399 and 401 eV for both 0.5CCN650 and CN550, which can be ascribed to the sp^2 hybridized aromatic N bonded to carbon atoms (C=N−C) and the tertiary N bonded to carbon atoms in the form of N–(C)$_3$. The binding energies of sp^2-bonded C and N both shift slightly to higher energies for 0.5CCN650, which can be attributed to more C=O and C−OH branched introduced into the CN matrix after the modification from KF.

Fig. 6a and d are the SEM images for the KF. KF was obtained by removing the kapok seed after collection as an inset in Fig. 6a. The KF is unstable under the irradiation of electron beams as shown in Fig. 6b,

which confirms that the facile carbonization temperature for the KF (Fig. 2b). The pristine CN from melamine is slabby while the KF modified CN is fluffy and easily scattered. As we can see from the SEM images for CN600 (Fig. 6b and e) and 2.5 CCN600 (Fig. 6c and f), CN600 shows stacked sheet-like structure. On the other hand, the 2.5CCN600 displays tremella-like nanostructures with apparent rolling lamellas. Both the specific surface area (S_{BET}) and pore volume are higher for sample 2.5CCN600 (48.0 $m^2 g^{-1}$, 0.46 $cm^3 g^{-1}$) than the CN600 (39.2 $m^2 g^{-1}$, 0.21 $cm^3 g^{-1}$). It is worth noting that 300 mg of 2.5CCN600 (inset in Fig. 6c) shows a larger volume than that for 300 mg of CN600 (inset in Fig. 6b). The microstructures are consistent with the S_{BET} and the pore volume from N_2 absorption (Figure S1 and Table S1). The SEM-EDS analysis in Figure S2 confirms the existence of C, N and O elements in 2.5CCN600 and CN600. Additionally, the thickness of the nanosheets in sample 0.5CCN650 and CN550 is investigated by AFM as shown in Figure S3. The average thickness is found to be in the range of 4.0 to 6.7 nm for 0.5CCN650, which is much thinner than that of CN550 (from 61.7 to 127.2 nm).

The TEM for CN600 in Fig. 7a and d reveal the high crystallization for CN600. However, 2.5CCN600 and 7.5CCN600 are more amorphous as seen in Fig. 7b and c. Both 2.5CCN600 and 7.5CCN600 exhibit the amorphous nano-biochar ribbon edges which are evenly distributed within CN. In HRTEM images (Fig. 7d–f), lattice fringes are clearly observed for CN600, with the lattice spacing of 0.3 nm assigned to the (002) planes. On the contrary, no obvious crystal lattice can be resolved on the edge of samples 2.5CCN600 and 7.5CCN600, which indicates the amorphous structures after the KF modification.

The TEM and scanning transmission electron microscopy high-angle annular dark-field imaging (STEM-HAADF) images for 1.5CCN650 with Pt particles are presented in Fig. 8. When the H_2PtCl_6 concentration is low, the Pt particles are preferably loaded on the edge of 1.5CCN650 and the size is approximately 2 nm (Fig. 8c and the inset). However, when we triple the amount of H_2PtCl_6, the Pt particles aggregate into larger particles that can be distinguished from the STEM-HADDF in Fig. 8d. Therefore, the bio-char ribbon edges are assumed to generate after the decomposition of KF, which can work as the substrate for the epitaxial growth of CCN. The higher density of Pt particles on the edges implies the selective loading of Pt particles, revealing the difference between nano-biochar and CN. Therefore, the results further confirm
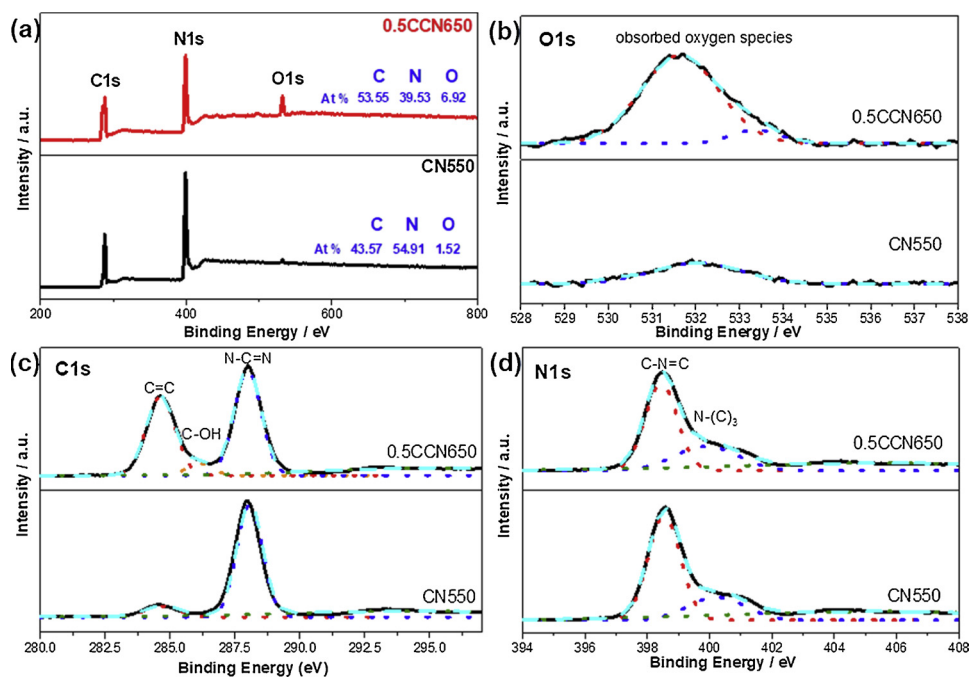
Fig. 5. The survey (a) and high-resolution XPS spectra of 0.5CCN650 and CN550 samples (b) O1s, (c) C1s, (d) N1s (The black lines are experimental peaks, the blue dash lines are fitting peaks and the dot lines are deconvolution peaks) (For interpretation of the references to colour in this figure legend, the reader is referred to the web version of this article).
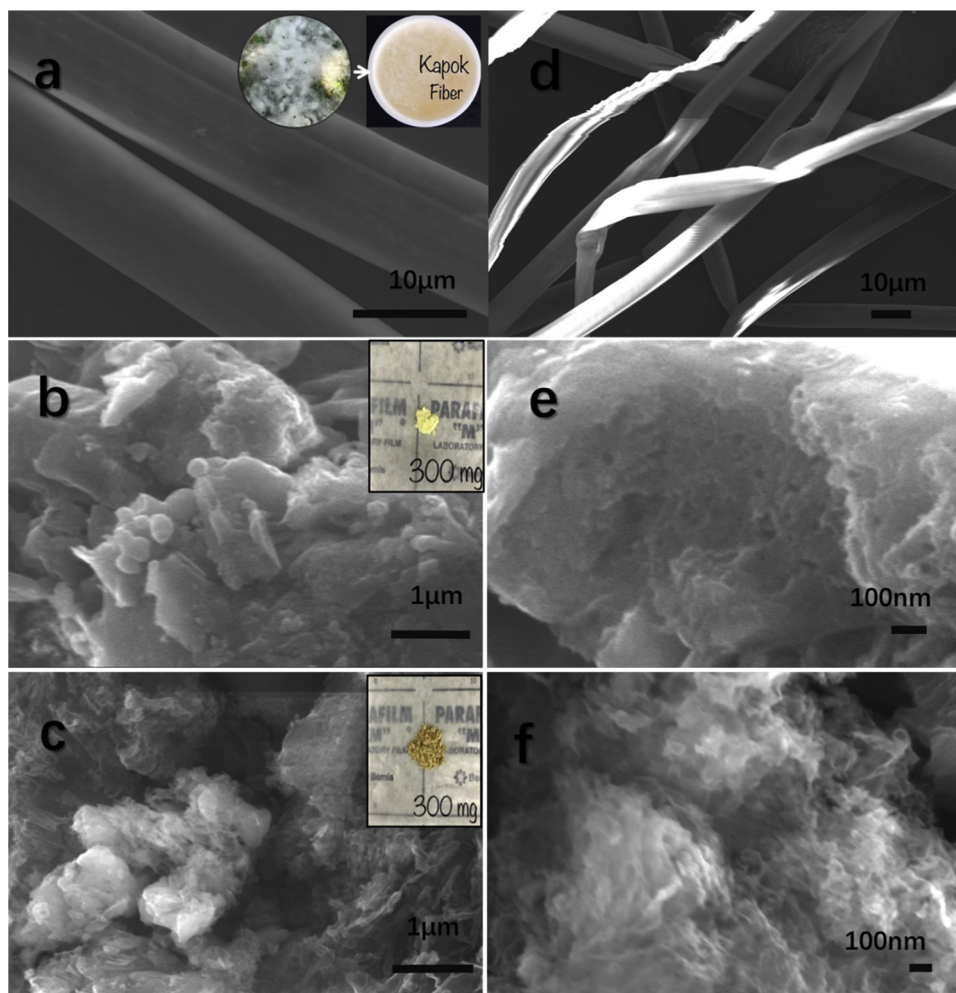

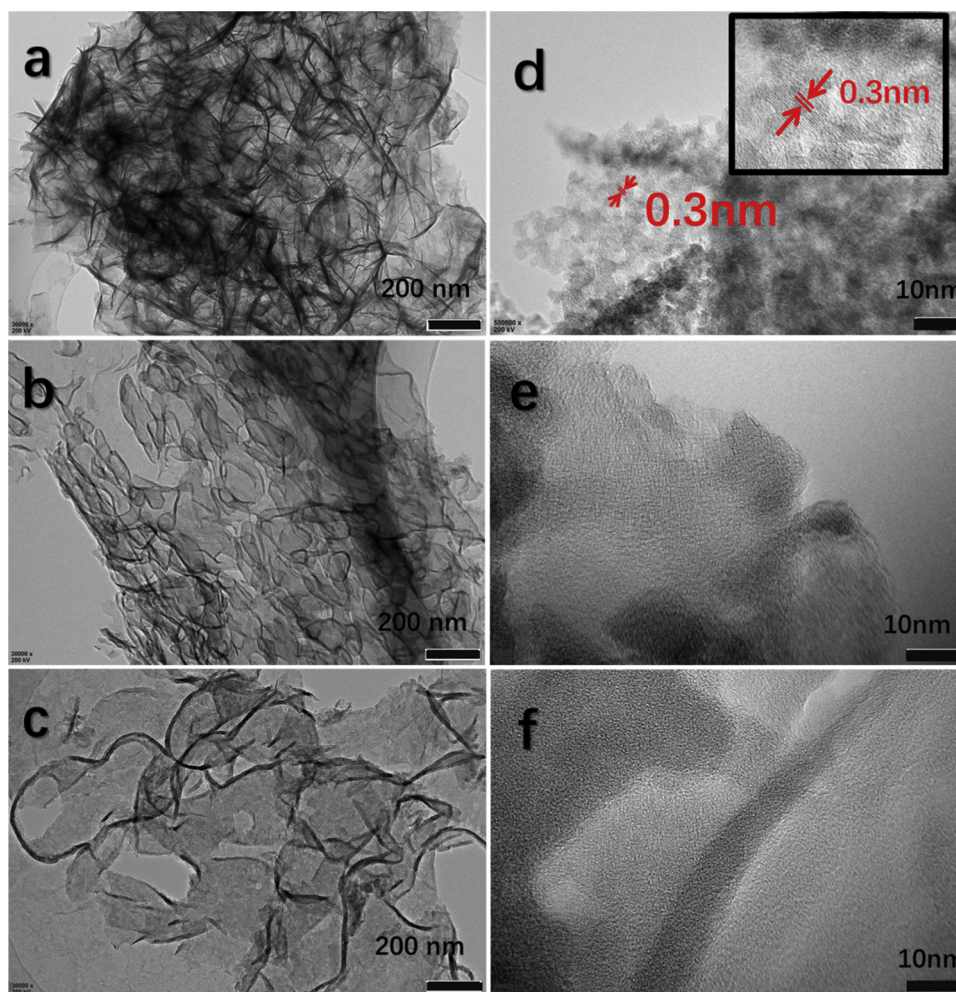**Fig. 6.** SEM images for KF (a, d), sample CN600 (b, e) and 2.5CCN600 (c, f).

Fig. 7. TEM (a, b, c) and HRTEM (d, e, f) images for sample CN600, 2.5CCN600 and 7.5CCN600.

the hypothesis of epitaxial growth of CCN on the nano-biochar ribbon which is derived from the KF pyrolysis.

4.2. Characterization of H_2 evolution performance from water splitting

Fig. 9 shows the water-splitting H_2 evolution results from all prepared photocatalysts under the visible light irradiation. It is clear that the H_2 evolution dramatically increases after the KF modification on CN. The H_2 generation rate of bare CN prepared at 550, 600 and 650 °C is 0.28, 0.97 and 4.06 μmol h^{-1}, respectively. The calcination temperature increases every 50 °C, the H_2 evolution amount increase fourfold accordingly. The optimal H_2 evolution rate for CCN prepared at different temperatures is 3.32, 6.38 and 18.89 μmol h^{-1} from 5CCN550, 2.5CCN600 and 1.5CCN650 accordingly. Therefore, the optimized sample 1.5CCN650 emitted 67.5 times H_2 than the CN from 550 °C under the visible light irradiation. Actually, KF as a biomass to modify CN is not a single factor. As reported in the literature [35,36], researchers studied the influence of pretreated KF (which was treated with a NaClO$_2$ solution) on the catalytic activity of CN. We also did the modification with the pretreated KF. In addition, we modified CN with the paraffin, which is the main component of the surface biomass wax. From Figure S4, we can see that both the cellulose and the paraffin have a positive impact on the catalytic activity. Interestingly, the synergistic effect has been realized in the KF modified CN, as 2.5CCN600 has the highest H_2 generation rate among compared samples.

Being different from the typical Gaussian distribution of a single influence factor [43], the influence of KF on the H_2 evolution exhibits irregular distribution. Herein, we first use the Game Theory to explain the distribution of the KF influence on the catalytic activity. The cellulose and paraffin are two variables in the KF system. The impact on the catalytic activity from the cellulose and paraffin are in Nash Equilibrium in this system. When the cellulose (or paraffin) amount locates in the positive loading range, while paraffin (or cellulose) locates in the scope of general effect, the resulting overall KF effect is moderate. Another situation, both the cellulose and paraffin amount locate in the general effect and the resulting overall effect on catalysis is also moderate. Alternatively, both the cellulose and paraffin locate in the positive doping range and the overall effect on the catalysis is optimized and vice versa. The observed non-Gaussian distributions in Fig. 9 are believed to result from the interplay of two influence factors. Therefore, the Game Theory Nash equilibrium well explains the random variation in H_2 evolution rate as the function of the KF amount.

The comparison on photocatalytic H_2 evolution of 1.5CCN650 with previously reported g-C$_3$N$_4$ modified by carbon materials is summarized in Table 1. Note that many factors will affect the hydrogen evolution rate, such as the dosage, the light power density and the temperature etc. It can be found that our 1.5CCN650 shows prominent photocatalytic H_2 evolution rate under visible light irradiation. Different from graphene, carbon quantum dots obtained from the complex process and other chemical carbon sources, the bio-mass KF is natural carbon source without pre-treatment, which highlights its great potential from environmental point of view.
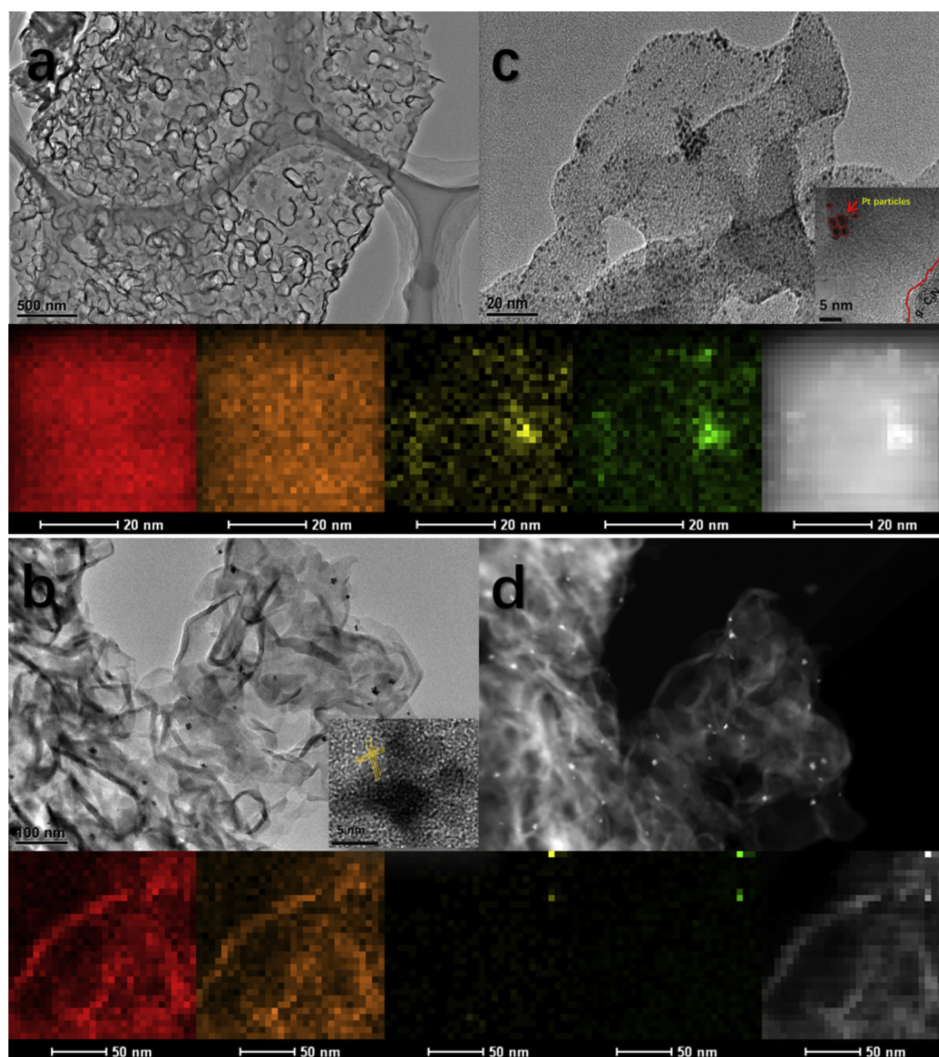
Fig. 8. TEM (a) and HRTEM (c) for 1.5CCN650 sample after loading Pt (3 g/L) and the corresponding EDS mapping for C-k (red), N-k in (orange), Pt-l (yellow) and Pt-m (green) and EDS mapping-STEM HAADF; the TEM (b) and HAADF (d) for 1.5CCN650 sample after loading Pt (10 g/L) and the corresponding EDS mapping for C-k (red), N-k in (orange), Pt-l in (yellow) and Pt-m (green) and the EDS mapping-STEM HAADF (For interpretation of the references to colour in this figure legend, the reader is referred to the web version of this article).

4.3. Mechanism of the photocatalytic water splitting to H_2 evolution

ESR spectra of CN550 and 0.5CCN650 show one single Lorentzian line, which is induced by the unpaired electrons on the carbon atoms of the heptazine rings [22] (Fig. 10a). The ESR intensity of 0.5CCN650 is similar to that of CN550, suggesting that no more vacancy is generated on the CN ring after the KF modification. However, the peak-to-peak width ($\triangle$Hpp) for the first differential curve from 0.5CCN650 is narrower as compared to that from CN550, which indicates electrons in 0.5CCN650 response faster to the change of ambient electromagnetic wave. Therefore, electrons are more movable in the 0.5CCN650 matrix. This built flexible electron transmission environment implies a higher photocatalytic activity for sample 0.5CCN650.

ESR spectroscopy followed by radicals trapping has been performed to determine the free radicals $\cdot O_2^-$ and $\cdot OH$ in methanol and water solution respectively, which are activated by the CN under visible-light irradiation (Fig. 10b). In the dark condition, no signals can be observed for both 0.5CCN650 and CN550, which indicate neither $\cdot O_2-$ nor $\cdot OH$ radicals are generated in the dark. After 10-minute visible-light irradiation, intensive $\cdot O_2-$ signal and moderate $\cdot OH$ signal are observed for both 0.5CCN650 and CN550. The generated $\cdot OH$ from the conversion of water or OH- by h^+ is relatively lower in 0.5CCN650 compared to

CN550, which is probably due to the h^+ in 0.5CCN650 are relatively poor transferred out to the interface to oxidize the water or OH- into $\cdot OH$. In contrast to the weak $\cdot OH$ signal, $\cdot O_2-$ signal is much stronger for 0.5CCN650 compared to CN550. The stronger $\cdot O_2-$ signals indicate that more electrons are transferred to the interface and then reduce the O_2 into $\cdot O_2-$. As the thin layered character for 0.5CCN650, the shortened perpendicular migration distance of charge carriers from the bulk to the surface is realized. We propose that the nano-biochar ribbon edges in 0.5CCN650 serve as the electron transfer-channel which increases the electron transfer rate and transition efficiency. Moreover, the selective loading of Pt on the nano-biochar ribbon edges in Fig. 8c further suggests the electron transfer-channel function of biochar. Therefore, greatly increase in photocatalytic H_2 evolution is realized in 0.5CCN650.

Time-resolved PL spectra (Fig. 10c) are also used to study the charge transfer properties for carbon nitride. The results show that the emission lifetime of 0.5CCN650 is longer than that of CN550. Such photogenerated electrons with a longer lifetime can boost surface reactions and therefore give rise to the enhanced photocatalytic activity [55]. Additionally, a large increase of the transient photocurrent of 1.5CCN650 compared to CN550 (Fig. 10d) also reveal large mobility of the photogenerated charge carriers, which explain a better
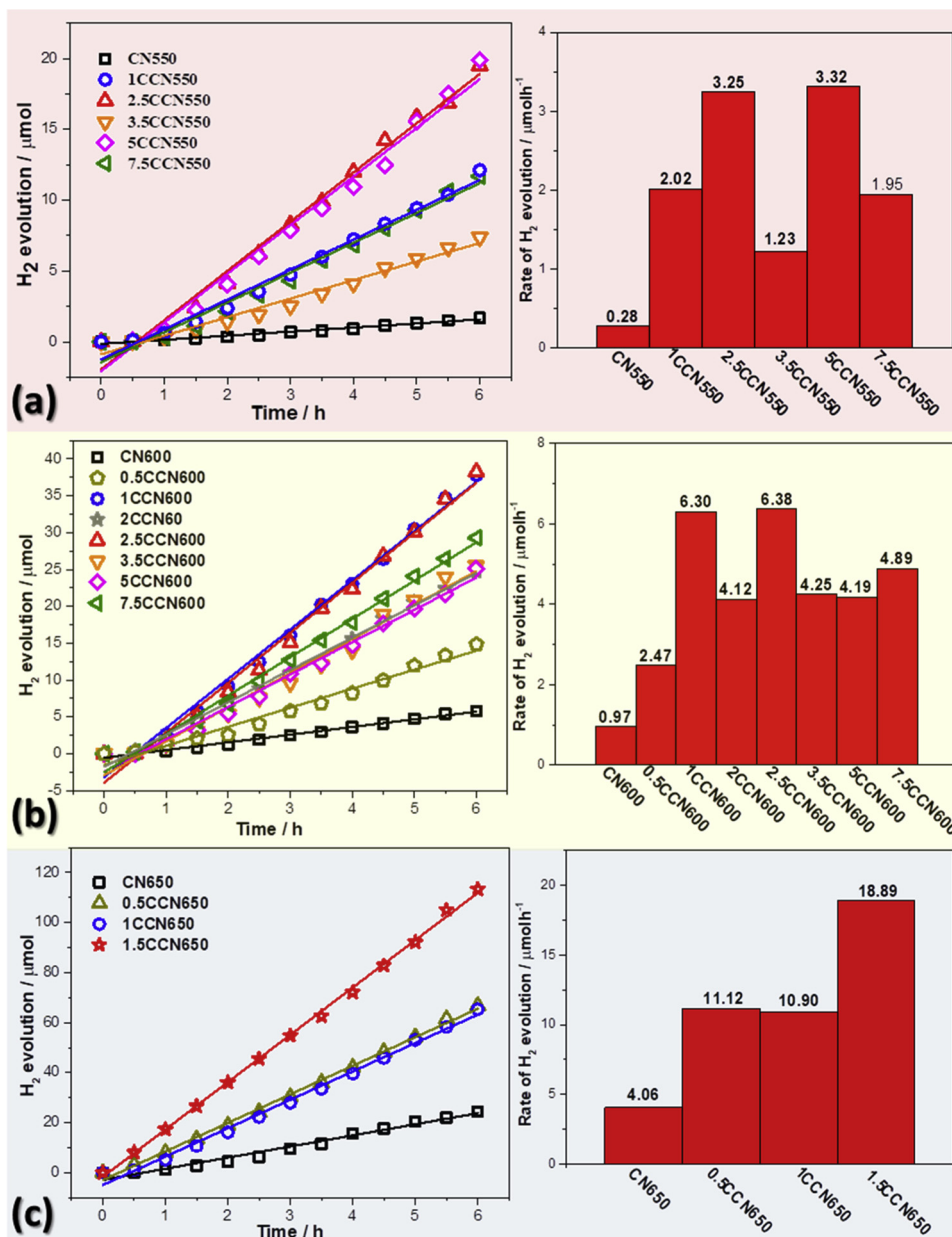
Fig. 9. Photocatalytic H_2 generation of carbon nitride (CN) and KF modified CN samples prepared at different temperatures under visible-light irradiation in 6 h; and the corresponding H_2 evolution rate (a, 550 °C; b, 600 °C; c, 650 °C).

Table 1
Hydrogen evolution rate and specific test conditions for the reported carbon modified CN under visible light irradiation. ('/' means the specific information is not provided).

| Samples	Photocatalyst dosage (mg)	Cocatalyst	Light power density (mW/cm^2)	Hydrogen evolution rate (μmol/h)	AQY at λ 420 nm	Promotion index compared with the pristine sample	Year Ref.
1.5CCN650	10	Pt	100	18.89	4.1%	67.5	This work
Carbon black modified g-C$_3$N$_4$	10	Pt	100	2.34	/	1.43	2018 [45]
g-C$_3$N$_4$@N-rich C nanofiber	10	Null	/	168.85	14.3%	18.3	2016 [46]
CDots-C$_3$N$_4$ composite	80	Null	/	46	16%	/	2015 [27]
carbonaceous material/g-C$_3$N$_4$	10	Pt	100	14.08	1.05%	35	2018 [47]
NiS-MoS$_2$/CNTs/CN	20	MoS$_2$ and NiS	100	6.198	/	/	2018 [48]
C-Modified g-C$_3$N$_4$	50	Pt	250	81.82	/	2.97	2018 [49]
Graphene/C$_3$N$_4$ composite	80	Pt	180	36.08	2.6%	3.07	2011 [50]
protonated GCN-rGO composite	100	/	/	55.7	/	10.02	2016 [51]
Carbon fiber/ g-C$_3$N$_4$ composite	50	Pt	180	54	/	4.6	2015 [52]
CQD-implanted g-C$_3$N$_4$ nanotubes	50	Pt	/	176.92	10.94 %	2.4	2018 [53]
Phosphorus-doped tubular CN/GQD composite	100	Pt	/	112.1	/	9	2018 [54]
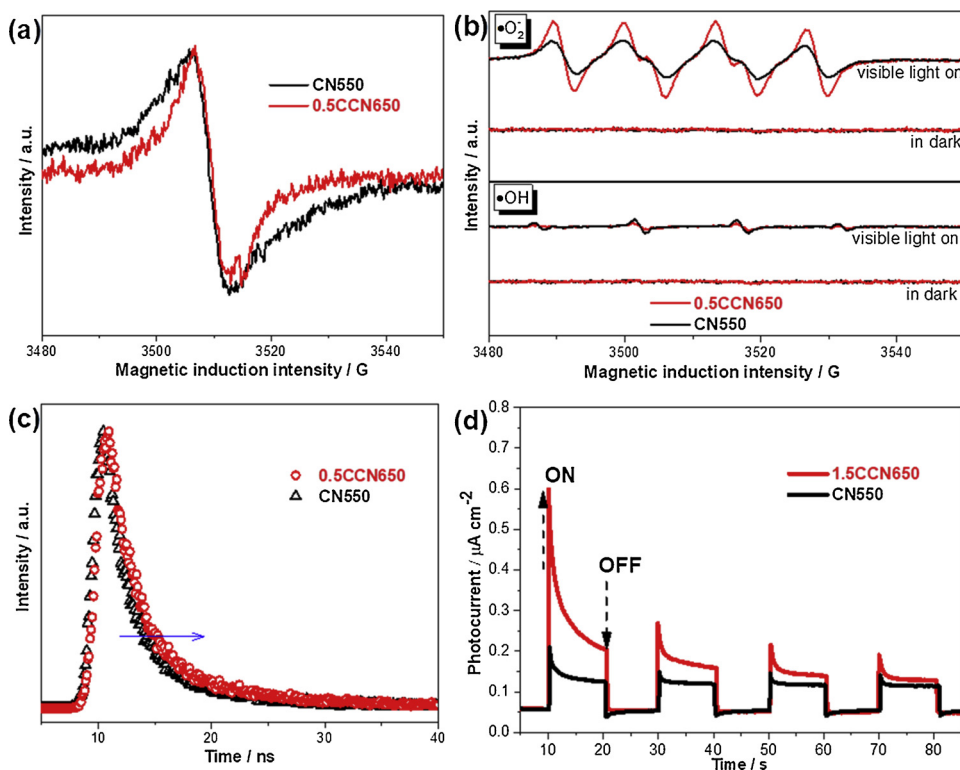
Fig. 10. (a) Room temperature ESR spectra for the CN550 and 0.5CCN650 in dark. (b) ESR spectra for sample CN550 and 0.5CCN650 in the dark and under visible light irradiation with DMPO-Methanol for testing the $\cdot O_2^-$ radicals and DMPO-H_2O for testing the $\cdot OH$ radicals. (c) Time-resolved PL spectra for sample CN550 and 0.5CCN650. (d) Transient photocurrent response of 1.5CCN650 and CN550 under the Xe lamp with 0.1 V bias voltage condition, 0.1 M Na_2SO_4 was used as the electrolyte.

photocatalytic performance of 1.5CCN650.

UV-Vis DRS in Fig. 11a shows the typical semiconductor optical absorption for CN650 and CCN650 samples, where the absorption edge is located at about 560 nm. The optical bandgap values (inset in Fig. 11a) are obtained from the generated Tauc plots by extrapolating the slope of the linear region to the x-axis [44]. The near infrared ray (NIR) absorption observed in the CCN650 samples is attributed to the delocalization of π electrons in the layered nanosheets [56]. The absorption edge red shifted upon an increase in the doping amount, a similar trend observed in the CCN prepared from 550 °C and 600 °C. (Figure S5) Therefore, the incorporation of carbon from carbonization of KF into the CN matrix results in the narrowing of the band-gap and the increase of the absorption over the entire wavelength range. The CN550 shows a bandgap of 2.65 eV, which agrees with the previously
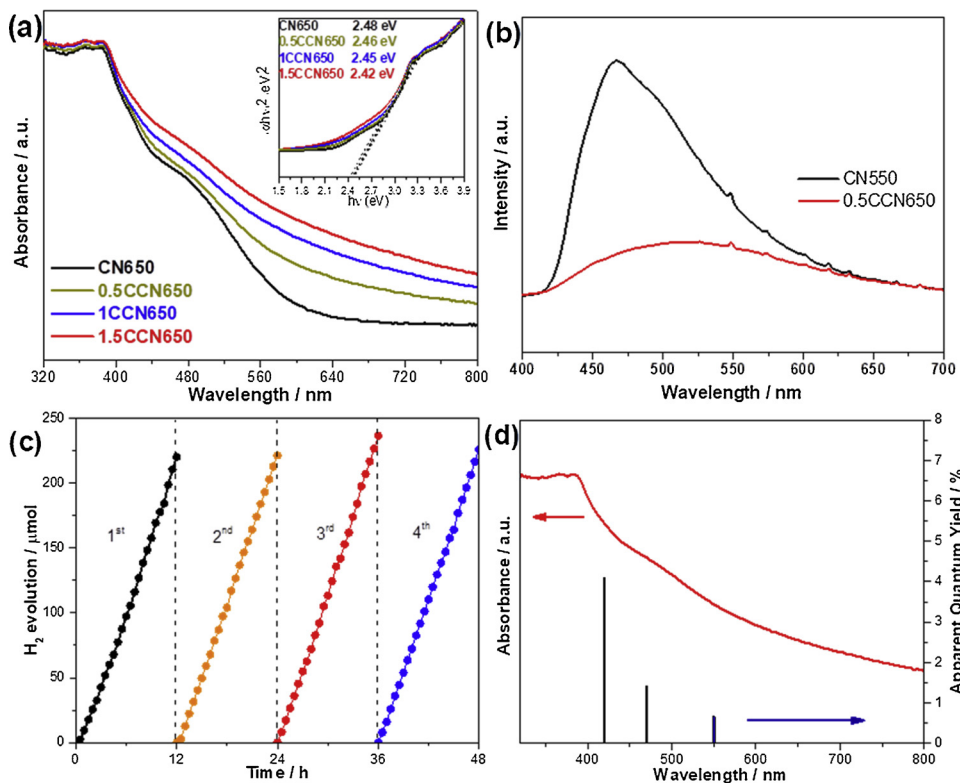

Fig. 11. (a) UV–vis DRS of CN650, 0.5CCN650, 1CCN650 and 1.5CCN650, the inset shows bandgap analysis through the modification of the Kubelka-Munk function. (b) The steady-state PL spectra for CN550 and 0.5CCN650. (c) The 48 h cycle measurement of 1.5CCN650 sample under visible light illumination (λ > 420 nm). Condition 10 mg catalyst, 10% v/v 100 mL TEOA aqueous solution, 100 μL 3% H_2PtCl_6. (d) The AQY against the light absorption wavelength of 1.5CCN650.

reported value [14]. The CN prepared at higher temperatures and the carbon doped CN samples show a steady decrease in the bandgap values of 2.48, 2.46, 2.45 and 2.42 eV for CN650, 0.5CCN650, 1CCN650 and 1.5CCN650, respectively. The increase in absorption toward higher wavelength and the narrowing bandgap indicate that the photocatalysts can absorb and utilize more low energy photons. Therefore the improvements in the photocatalytic H_2 are observed in CN600, CN650 and the CCNs. The steady-state PL for CN and CCNs are provided in Fig. 11b and Figure S6. Upon the excitation with 325 nm, the CN samples exhibit strong emission centered at 470 nm. When carbon introduced into the CN matrix, the PL not only redshifts to approximately 520 nm but also decreases in intensity for all CCN samples. The emission peaks for CN can be ascribed to the band-band PL phenomenon with the energy of light approximately equal to the bandgap energy of CN [18]. Therefore the red-shift for 0.5CCN650 is in agreement with the decreased bandgap obtained from DRS. In addition, the decrease in PL intensity in the CCN samples implies (1) the partial amorphism of CCN structure derived from the KF modification induces the nonradiative recombination sites in CN matrix. (2) the exciton dissociation is facilitated on the nano-biochar ribbon edge. The former effect was supposed to reduce the overall photocatalytic activity. On the other hand, the latter one should exert a positive impact on the improvement of photocatalytic activity [57], which is therefore believed to be dominant in the KF modified samples.

CN is thermally stable up to ca. 600 °C in the air, as evidenced by TGA [14]. The TGA for the comparison of the stability of KF modified CN and CN is provided in Figure S7. The thermal stability for CCN was overall well-kept after the KF modification. Moreover, the stability of sample 1.5CCN650 under the visible light condition was also tested. Clearly, the H_2 generation is quite stable under 4 times' circulation, reflecting the good stability of catalyst 1.5CCN650 (Fig. 11c). As we can see the yield of H_2 steadily increases in the second and third round as compared to the first cycle and then falls back in the fourth cycle. This phenomenon is presumably caused by the change of TEOA amount. In the first round, TEOA is full-dose, therefore the excess TEOA molecules are involved in the reflection and absorption of the incident photons. With the evolving of the experiment, the excess TEOA is gradually subdued; the impact of excess TEOA on H_2 generation is relieved so the H_2 amount increases in the 2nd and 3rd round steadily. With the further reduction of TEOA in the 4th cycle, the insufficiency of the sacrificial agent would induce the combination of charge carriers, which results in the reduction of H_2 evolution. Moreover, the TEM image of 1.5CCN650 sample after the stability test is provided in Figure S8. The layered structure with nano-biochar ribbon edges is well maintained after the H_2 evolution experiments. The darker spots located on the nano-biochar ribbon edges with slight stripes shape are not observed on the initial 1.5CCN650 and therefore are supposed to be the Pt particles loading along the texture of the nano-biochar. The AQYs of sample 1.5CCN650 are 4.1%, 1.4% and 0.66% at 420 nm, 470 and 550 nm, respectively (Fig. 11d). The variation of the AQY is in good accordance with the absorption spectrum of 1.5CCN650, indicating that the photoexcitation upon 1.5CCN650 promotes the H_2 formation.

The Fermi Level (E_f) for CN is assumed to be 0 eV according to

literature [17,57]. So, the VB-XPS spectra (Fig. 12a) reveal that the energy gap between the valence band maximum (VBM) and E_f is 2.01 eV and 1.90 eV for the 0.5CCN650 and CN550, respectively. Therefore, according to the bandgap energy (E_g) from DRS, the conduction band minimum (CBM) of the 0.5CCN650 and CN550 is calculated to be -0.45 eV and -0.75 eV, respectively. The energy band alignments of the 0.5CCN650 and CN550 are illustrated in Fig. 12b. It is seen that both VBM and CBM shift to more positive potential after the KF modification. The VBM for CN550 is more aligned with the $OH^-/\cdot OH$ redox potential than that of 0.5CCN650, which is consistent the stronger ESR signal of CN550 sample when testing the generated hydroxyl radicals. The more positive CBM for 0.5CCN650 is quite aligned with the redox potential for H^+/H_2, which results in a shorted conversion path for the photogenerated electrons [44]. Moreover, the bio-char ribbon edges can serve as the channel for electron transfer which facilitates the electron transmission from photocatalyst to Pt and then finally to H^+ reduction. Therefore the improved photocatalytic H_2 evolution can be obtained in 0.5CCN650.

5. Conclusion

In conclusion, KF as a biomass carbon resource has been used directly for the modification of CN in this work. The CN thin layers are epitaxially grown on the nano-biochar ribbon edges derived from the pyrolysis of KF. Therefore, KF not only serves as the carbon resource but also the substrate for the growth of CN. The prepared CCN composites exhibit booming photocatalytic H_2 generation. The optimal sample shows 67.5 times H_2 generation than the pristine CN in 6 h under visible-light irradiation. The CCN composites present narrower bandgaps and wider light absorption region, with the higher S_{BET} and the pore volume which can provide more H^+ reduction sites. Moreover, CCNs have shortened perpendicular migration distance of charge carriers from the bulk to the surface, which accelerates the electron transport along the in-plane direction [19]. At last, the AQYs are calculated to be 4.1%, 1.4%, 0.66% for monochromatic light $\lambda = 420$ nm, $\lambda = 470$ nm and $\lambda = 550$ nm, respectively. Therefore, the reported strategy opens a new prospect to utilize the KF as a cost-effective, biocompatible, eco-friendly carbon source in photocatalysis.
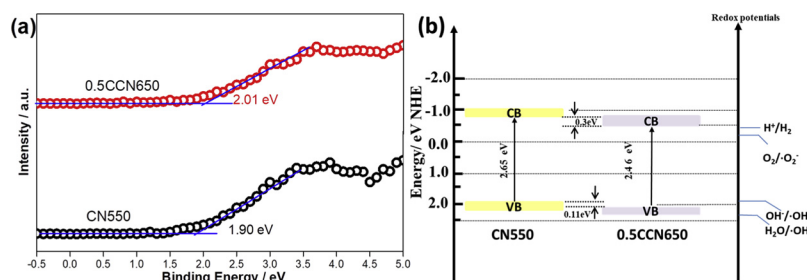
Fig. 12. (a) VB-XPS spectra, (b) Schematic band structure evolution of 0.5CCN650 compared with CN550.

Appendix A. Supplementary data

Supplementary material related to this article can be found, in the online version, at doi:https://doi.org/10.1016/j.apcatb.2019.01.040.

References

[1] T. Lin, C. Yang, Z. Wang, H. Yin, X. Lü, F. Huang, J. Lin, X. Xie, M. Jiang, Energy Environ. Sci. 7 (2014) 967–972.

[2] Y. Yang, L.-C. Yin, Y. Gong, P. Niu, J.-Q. Wang, L. Gu, X. Chen, G. Liu, L. Wang, H.-M. Cheng, Adv. Mater. 30 (2018) 1704479.

[3] X. Liu, G. Zhu, X. Wang, X. Yuan, T. Lin, F. Huang, Adv. Energy Mater. 6 (2016) 1600452.

[4] D. Ma, J.-W. Shi, Y. Zou, Z. Fan, X. Ji, C. Niu, ACS Appl. Mater. Interfaces 9 (2017) 25377–25386.

[5] S. Le, T. Jiang, Y. Li, Q. Zhao, Y. Li, W. Fang, M. Gong, Appl. Catal. B-Environ. 200 (2017) 601–610.

[6] U. Alam, A. Khan, W. Raza, A. Khan, D. Bahnemann, M. Muneer, Catal. Today 284 (2017) 169–178.

[7] M.A. Behnajady, N. Modirshahla, R. Hamzavi, J. Hazard. Mater. 133 (2006) 226–232.

[8] C.L. Yu, K. Yang, Y. Xie, Q.Z. Fan, J.C. Yu, Q. Shu, C.Y. Wang, Nanoscale 5 (2013) 2142–2151.

[9] W. Zhen, X. Ning, B. Yang, Y. Wu, Z. Li, G. Lu, Appl. Catal., B-Environ. 221 (2018) 243–257.

[10] D.P. Kumar, S. Hong, D.A. Reddy, T.K. Kim, Appl. Catal., B-Environ. 212 (2017) 7–14.

[11] M. Xing, B. Qiu, M. Du, Q. Zhu, L. Wang, J. Zhang, Adv. Funct. Mater. 27 (2017).

[12] R. Li, H. Han, F. Zhang, D. Wang, C. Li, Energy Environ. Sci. 7 (2014) 1369–1376.

[13] S. Wang, P. Chen, Y. Bai, J.-H. Yun, G. Liu, L. Wang, Adv. Mater. 30 (2018) 1800486.

[14] H. Zhang, L. Zhao, F. Geng, L.-H. Guo, B. Wan, Y. Yang, Appl. Catal. B-Environ. 180 (2016) 656–662.

[15] L. Jiang, X. Yuan, Y. Pan, J. Liang, G. Zeng, Z. Wu, H. Wang, Appl. Catal. B-Environ. 217 (2017) 388–406.

[16] Y. Zhang, J. Liu, G. Wu, W. Chen, Nanoscale 4 (2012) 5300–5303.

[17] H. Shi, G. Chen, C. Zhang, Z. Zou, ACS Catal. 4 (2014) 3637–3643.

[18] L. Zhang, L. Li, X. Sun, P. Liu, D. Yang, X. Zhao, Materials 9 (2016) 927.

[19] H. Ou, L. Lin, Y. Zheng, P. Yang, Y. Fang, X. Wang, Adv. Mater. 29 (2017) 1700008–17000013.

[20] K. Chen, X.-M. Zhang, X.-F. Yang, M.-G. Jiao, Z. Zhou, M.-H. Zhang, D.-H. Wang, X.-H. Bu, Appl. Catal. B-Environ. 238 (2018) 263–273.

[21] S. Gong, Z. Jiang, P. Shi, J. Fan, Q. Xu, Y. Min, Appl. Catal. B-Environ. 238 (2018) 318–327.

[22] G. Zhang, Q. Ji, Z. Wu, G. Wang, H. Liu, J. Qu, J. Li, Adv. Funct. Mater. 28 (2018) 1706462.

[23] W. Wang, G. Li, T. An, D.K.L. Chan, J.C. Yu, P.K. Wong, Appl. Catal. B-Environ. 238 (2018) 126–135.

[24] P. Zhou, J. Lai, Y. Tang, Y. Chao, F. Lin, S. Guo, Appl. Catal. B-Environ. 238 (2018) 161–167.

[25] Z. Jin, Q. Zhang, J. Chen, S. Huang, L. Hu, Y.-J. Zeng, H. Zhang, S. Ruan, T. Ohno, Appl. Catal., B-Environ. 234 (2018) 198–205.

[26] J. Liu, H. Xu, X. Xu, Y. Song, J. Lian, Y. Zhao, L. Wang, L. Huang, H. Ji, H. Li, Appl. Catal. B-Environ. 207 (2017) 429–437.

[27] J. Liu, Y. Liu, N. Liu, Y. Han, X. Zhang, H. Huang, Y. Lifshitz, S.-T. Lee, J. Zhong, Z. Kang, Science 347 (2015) 970–974.

[28] Y.Z. Hong, Y.D. Meng, G.Y. Zhang, B.X. Yin, Y. Zhao, W.D. Shi, C.S. Li, Sep. Purif. Technol. 171 (2016) 229–237.

[29] F. Wang, P. Chen, Y. Feng, Z. Xie, Y. Liu, Y. Su, Q. Zhang, Y. Wang, K. Yao, W. Lv, G. Liu, Appl. Catal. B-Environ. 207 (2017) 103–113.

[30] S. Fang, Y. Xia, K.L. Lv, Q. Li, J. Sun, M. Li, Appl. Catal. B-Environ. 185 (2016) 225–232.

[31] N. Bao, X. Hu, Q. Zhang, X. Miao, X. Jie, S. Zhou, Appl. Surf. Sci. 403 (2017) 682–690.

[32] R.L. Huang, W.Q. Huang, D.F. Li, L.L. Ma, A.L. Pan, W.Y. Hu, X.X. Fan, G.F. Huang, J. Phys. D Appl. Phys. 51 (2018) 135501–135508.

[33] Z.W. Tong, D. Yang, X.Y. Zhao, J.F. Shi, F. Ding, X.Y. Zou, Z.Y. Jiang, Chem. Eng. J. 337 (2018) 312–321.

[34] Z. Jin, J. Chen, S. Huang, J. Wu, Q. Zhang, W. Zhang, Y.-J. Zeng, S. Ruan, T. Ohno, Catal. Today 315 (2018) 149–154.

[35] Y. Cao, L. Xie, G. Sun, F. Su, Q.-Q. Kong, F. Li, W. Ma, J. Shi, D. Jiang, C. Lu, C.-M. Chen, Sustain. Energy Fuels 2 (2018) 455–465.

[36] M.A. Mohamed, M.F.M. Zain, L. Jeffery Minggu, M.B. Kassim, N.A. Saidina Amin, W.N.W. Salleh, M.N.I. Salehmin, M.F. Md Nasir, Z.A. Mohd Hir, Appl. Catal., B-Environ. 236 (2018) 265–279.

[37] J. Safaei, N.A. Mohamed, M.F. Mohamad Noh, M.F. Soh, N.A. Ludin, M.A. Ibrahim, W.N. Roslam Wan Isahak, M.A. Mat Teridi, J. Mater. Chem. A 6 (2018) 22346–22380.

[38] J. Bian, L. Xi, J. Li, Z. Xiong, C. Huang, K.M. Lange, J. Tang, M. Shalom, R.-Q. Zhang, Chem. – Asian J. 12 (2017) 1005–1012.

[39] X. Zhao, D. Pan, X. Chen, R. Li, T. Jiang, W. Wang, G. Li, D.Y.C. Leung, Appl. Surf. Sci. 467-468 (2019) 658–665.

[40] S. Cao, J. Low, J. Yu, M. Jaroniec, Adv. Mater. 27 (2015) 2150–2176.

[41] W. Cui, J.Y. Li, F. Dong, Y.J. Sun, G.M. Jiang, W.L. Cen, S.C. Lee, Z.B. Wulle, Environ. Sci. Technol. 51 (2017) 10682–10690.

[42] Y.Y. Kang, Y.Q. Yang, L.C. Yin, X.D. Kang, G. Liu, H.M. Cheng, Adv. Mater. 27 (2015) 4572–4577.

[43] L. Kong, Y. Ji, Z. Dang, J. Yan, P. Li, Y. Li, S. Liu, Adv. Funct. Mater. 28 (2018) 1800668–1800677.

[44] F. Wang, Y. Wang, Y. Feng, Y. Zeng, Z. Xie, Q. Zhang, Y. Su, P. Chen, Y. Liu, K. Yao, Appl. Catal., B-Environ. 221 (2018) 510–520.

[45] L. Zhang, Z. Jin, H. Lu, T. Lin, S. Ruan, X.S. Zhao, Y.-J. Zeng, ACS Omega 3 (2018) 15009–15017.

[46] H. Qing, W. Bing, G. Jian, Q. Liangti, Angew. Chem. Int. Ed. 55 (2016) 10849–10853.

[47] Z. Jin, J. Chen, S. Huang, J. Wu, Q. Zhang, W. Zhang, Y.-J. Zeng, S. Ruan, T. Ohno, Catal. Today (2018).

[48] Y.-X. Zhang, K. Li, Y.-X. Yu, W.-D. Zhang, J. Colloid Interface Sci. 526 (2018) 374–383.

[49] H. Wang, G. Huang, Z. Chen, W. Li, Catalysts 8 (2018) 366.

[50] Q. Xiang, J. Yu, M. Jaroniec, J. Phys. Chem. C 115 (2011) 7355–7363.

[51] C. Pu, J. Wan, E. Liu, Y. Yin, J. Li, Y. Ma, J. Fan, X. Hu, Appl. Surf. Sci. 399 (2017) 139–150.

[52] J. Zhang, F. Huang, Appl. Surf. Sci. 358 (2015) 287–295.

[53] Y. Wang, X. Liu, J. Liu, B. Han, X. Hu, F. Yang, Z. Xu, Y. Li, S. Jia, Z. Li, Y. Zhao, Angew. Chem. Int. Ed. 57 (2018) 5765–5771.

[54] Y. Gao, F. Hou, S. Hu, B. Wu, Y. Wang, H. Zhang, B. Jiang, H. Fu, Chemcatchem 10 (2018) 1330–1335.

[55] N. Meng, J. Ren, Y. Liu, Y. Huang, T. Petit, B. Zhang, Energy Environ. Sci. 11 (2018) 566–571.

[56] Nisha Prakash, Gaurav Kumar, Manjri Singh, Arun Barvat, Prabir Pal, Surinder P. Singh, H.K. Singh, Suraj P. Khanna, Adv. Opt. Mater. 6 (2018) 1800191–1800200.

[57] C.H. Choi, L. Lin, S. Gim, S. Lee, H. Kim, X. Wang, W. Choi, ACS Catal. (2018) 4241–4256.